HHS Public Access

Author manuscript

IEEE Trans Ultrason Ferroelectr Freq Control. Author manuscript; available in PMC 2019 May 01.

Published in final edited form as:

IEEE Trans Ultrason Ferroelectr Freq Control. 2018 May ; 65(5): 684–696. doi:10.1109/TUFFC.2018.2807765

Optimization of Transmit Parameters in Cardiac Strain Imaging with Full and Partial Aperture Coherent Compounding

Vincent Sayseng, **Julien Grondin**, and **Elisa Konofagou**

Member, IEEE

Abstract

Coherent compounding methods using the full or partial transmit aperture have been investigated as a possible means of increasing strain measurement accuracy in cardiac strain imaging; however, the optimal transmit parameters in either compounding approach have yet to be determined. The relationship between strain estimation accuracy and transmit parameters—specifically the subaperture, angular aperture, tilt angle, number of virtual sources, and frame rate—in partial aperture (subaperture compounding) and full aperture (steered compounding) fundamental mode cardiac imaging was thus investigated and compared. Field II simulation of a 3D cylindrical annulus undergoing deformation and twist was developed to evaluate accuracy of 2D strain estimation in cross-sectional views. The tradeoff between frame rate and number of virtual sources was then investigated via transthoracic imaging in the parasternal short-axis view of five healthy human subjects, using the Strain Filter to quantify estimation precision. Finally, the optimized subaperture compounding sequence (25-element subperture, 90° angular aperture, 10 virtual sources, 300 Hz frame rate) was compared to the optimized steered compounding sequence (60° angular aperture, 15° tilt, 10 virtual sources, 300 Hz frame rate) via transthoracic imaging of five healthy subjects. Both approaches were determined to estimate cumulative radial strain with statistically equivalent precision (subaperture compounding $E(SNRe|\varepsilon = 41\%) = 3.56$, and steered compounding $E(SNRe|\varepsilon = 41\%) = 4.26$).

Index Terms

cardiac strain imaging; coherent compounding; high frame rate imaging; ultrasound simulation; transthoracic imaging

I. Introduction

THERE has been considerable interest in developing quantitative approaches to assessing myocardial health with ultrasound. Much of this effort has been directed towards inventing or refining methods to measure stiffness or strain in the heart, as they are quantitative measures of the cardiac muscle's condition and have been associated with patient outcomes [1]–[4]. This study focuses on one cardiac strain imaging technique in particular, Myocardial Elastography (ME). ME uses normalized cross-correlation of RF signals to estimate displacement and strain in two-dimensions (2D) in an angle-independent fashion. By using RF data to estimate strains, as opposed to relying on the B-mode, ME leverages both phase and envelope information to accurately estimate displacement [5]. ME has been theoretically validated with a 3D finite-element model based on a normal and ischemic canine left

ventricle, and has been experimentally validated in vivo with tagged magnetic resonance imaging (tMRI) of a healthy human volunteer [6]. The capabilities of ME include localization of infarcts in a mice model [7], monitoring of ischemia progression in a canine model [8], monitoring of RF ablation therapy in both canines and human patients with atrial fibrillation [9], and differentiating ischemic patients from healthy individuals [10]. This study is focused on the application of ME to estimate radial and circumferential cardiac strain in the short-axis view.

The success of ME, as well as many strain imaging techniques, is reliant on high frame rate; an insufficient frame rate leads to estimator decorrelation due large interframe motion, leading to inaccurate strain estimation [2], [11]–[13]. Coherent compounding has been shown to be capable of producing B-mode images of comparable quality to those generated with focused transmits, while relying on fewer transmissions, thus enabling higher frame rates [14]–[21]. Compounding has been shown to improve strain estimation accuracy [18], [22], and is amenable to being implemented in conjunction with other strategies to improve strain imaging, such as harmonic imaging [23]. Compounding for cardiac imaging has been implemented in two main configurations. First, compounding can be performed with a partial transmit aperture and no steering of the diverging wave [16], [24], [25]. Second, compounding can be accomplished with a full transmit aperture and steering of the diverging wave [26]–[28]. Recently, compounding was shown to improve ME strain estimation performance in transthoracic imaging of the myocardium [29]. However, the best transmit parameters for a compounded diverging wave sequence that will maximize cumulative strain estimation accuracy are yet unknown.

This study aims to identify the optimal transmit parameters for the two approaches to coherent compounding—using partial and full transmit apertures—via simulation and transthoracic imaging of healthy subjects. Previous work by Nayak et al has concluded that a 13 element subaperture yields the most accurate strain estimation in carotid imaging with compounded diverging waves [30]. Echocardiography, however, offers a number of unique challenges, including a small imaging window, susceptibility to artifacts originating from the ribs or neighboring organ systems, and a large depth requirement. To overcome these challenges, it is critical that the imaging sequence used is optimized to estimate strain as accurately as possible. Previously, we have performed investigations into the effect of subaperture, angular aperture, and virtual source number on strain estimation accuracy in partial transmit compounding [24], [29]. However, no extensive investigation into the best transmit parameters for strain estimation of the myocardium with full transmit aperture compounding has yet been performed, nor has any comparison between the two approaches to compounding yet been accomplished. The three parameters to be investigated in partial transmit aperture compounding (referred to as *subaperture compounding* in this paper) are the subaperture, angular aperture, and number of virtual sources. In full transmit aperture compounding (referred to as *steered compounding* herein), the parameters of interest are angular aperture, tilt angle, and number of virtual sources. Simulations were employed to investigate strain estimation accuracy, while a quantitative investigation into transthoracic cardiac strain was designed to assess strain estimation precision. A range of subaperture, angular aperture, and tilt angle values are evaluated in simulations to determine the configurations that yield the most accurate cumulative strain estimation. The best transmit

parameters for both sequences are then integrated into a custom sequence designed to compare different frame rate and virtual source number configurations at a PRF of 3000 Hz: 50 Hz/60 sources, 100 Hz/30 sources, 200 Hz/15 sources, 300 Hz/10 sources, 500 Hz/6 sources. Finally, the optimized subaperture compounding sequence will be directly compared against the optimized steered compounding sequence via transthoracic imaging of five healthy subjects.

II. Methods

A. Transmit parameters for coherent compounding

Diverging waves were generated by setting virtual sources behind the element array. Compounding with diverging waves was achieved with two different transmit strategies, dependent on whether the transmit aperture was partially or fully activated during emission.

The first transmit strategy that was employed utilized a partial transmit aperture. Fig. 1 illustrates the three critical transmit parameters: the number of virtual sources, subaperture size, and angular aperture. The number of virtual sources dictated the number of transmits to be coherently compounded, and the distance of the virtual sources from the element array was defined by the subaperture size and angular aperture. Subaperture was defined as the number of elements activated during transmission (which may be expressed as a percentage of the available transmit aperture). Virtual sources were centered over the subaperture. Virtual source pitch was maximized. Note that the distance between the first and last virtual sources (i.e. the virtual aperture) decreases as the subaperture increases. Since this transmit strategy constrains the virtual source to be centered over the subaperture, the diverging waves emitted with this scheme are not steered.

Figs. 2 and 3 summarizes the PSFs and normalized pressure plots of various transmit configurations for subaperture and steered compounding, respectively. Increasing the virtual aperture leads to an improvement in sonographic resolution (Fig. 2a) at the cost of reducing transmitted pressure (Fig. 3a). Angular aperture Φ is defined as follows:

$$\Phi = 2\arctan\left(\frac{a}{2d}\right), \quad (1)$$

where a is the width of the transmit aperture, and d is the distance of the virtual sources from the element array. An increase in Φ leads to an improvement in resolution (Fig. 2b), but reduces transmitted pressure (Fig. 3b).

An alternative compounding transmit strategy is to utilize the full transmit aperture. Fig. 1 illustrates the three critical transmit parameters: the number of virtual sources, angular aperture, and tilt angle. The relationship between the angular aperture Φ and the tilt Θ with the axial z_{vs} and lateral x_{vs} position of the virtual sources and aperture a is summarized as follows [26]:

$$\tan\left(\Theta \pm \frac{\Phi}{2}\right) = \frac{\pm a + 2x_{vs}}{-2z_{vs}}. \quad (2)$$

As in subaperture compounding, increasing Φ in steered compounding leads to an improvement in resolution (Fig. 2c) at the cost of transmitted pressure (Fig. 3c). Increasing Θ improves resolution (Fig. 2d) at the cost of transmitted pressure (Fig. 3d). Since the full transmit aperture is utilized, transmits from virtual sources located beyond the centerline of the array will generate a steered diverging wave.

B. Simulation of the left-ventricular contraction

A cylindrical annulus undergoing symmetric radial thickening was generated to simulate parasternal short-axis cross-sectional views of the systolic left ventricle. Field II was used to generate the RF data based on a simulated cardiac phased array (2.5 MHz center frequency, 64 elements, 0.32 mm pitch) and a normally distributed scatterer distribution [31]. The mean amplitude of the annulus scatterers was four times greater than that of the background scatterers. The attenuation coefficient was 0.54 dB/cm/MHz, the soft tissue average [32]. The annulus center was placed at a depth of 60 mm. The annulus had a radial thickness of 10 mm and outer diameter of 50 mm, and underwent deformation and translation with rotation over the duration of simulated systole: 1.5 mm radial displacement of outer (epicardial) wall towards annulus center, 4.5 mm radial displacement of inner (endocardial) wall towards annulus center, 3.0 mm displacement of the phantom out-of-plane, and epicardial and endocardial rotation of 4° and 8°, respectively. At end-systole, the annulus had a total cumulative radial thickening of 30%. Simulated myocardial strain, displacement, and torsion was within known physiological bounds [33]–[36]. Background scatterers were simulated as static over the duration of systole. For all compounding strategies simulated, 450 frames were acquired over systole, generating 30 compounded acquisitions with 15 virtual sources each. Interframe motion was simulated between each virtual source transmit. In order to simulate decorrelation, white noise was bandlimited (cutoff frequencies of 1.5 MHz and 4 MHz) to match the frequency spectrum of the simulated P4-2 probe. The resulting noise signal was added to the RF signal; note that the noise signal was randomized from a normal distribution between individual transmit acquisitions (as opposed to randomizing between compounded acquisitions).

A 1D normalized cross-correlation kernel was applied to the beamformed RF signals in a 2D search to determine axial and lateral displacements [6]. The window size was 4.4 mm with a 0.44 mm window shift (10% overlap); 10 lines were linearly interpolated between adjacent RF lines before lateral displacements were estimated [6]. A recorrelation method was implemented to refine the lateral displacement estimation [6]. Cosine interpolation was applied to the cross-correlation peak to obtain sub-sample axial and lateral displacements [6]. Interframe displacements were integrated over time, and a least squares strain estimator was used to calculate the resulting cumulative strains using a window of 3.9 mm by 4.0° [37]. The resulting axial and lateral strains were converted from a polar to Cartesian

coordinate system. Radial cumulative strains were estimated from the 2-D strain tensor. A median filter of 7.2 mm by 7.5° was used to smooth strains.

In order to evaluate strain estimation accuracy, theoretical end-systolic cumulative axial, lateral, and radial strains (ε) were calculated throughout the entirety of the virtual phantom walls over all 30 frames of systole. Estimated end-systolic cumulative strains ($\hat{\varepsilon}$) were compared with the theoretical end-systolic strain, expressed as normalized strain error (%), or $\Delta\hat{\varepsilon}$:

$$\Delta\hat{\varepsilon}(\%) = \frac{\sum(\varepsilon - \hat{\varepsilon})^2}{\sum \varepsilon^2} * 100. \quad (3)$$

In order to reduce the effect of boundaries, only $\hat{\varepsilon}$ within a masked area was considered. The mask was a 6.5 mm thick annulus overlaid onto the center of the simulated ventricle.

Both subaperture and steered compounding sequences were simulated, with the goal of determining the optimal transmit parameters. For subaperture compounding, subaperture and angular aperture were investigated. Maintaining the number of virtual sources at 15 and angular aperture at 90°, subapertures ranging from 5 through 64 elements (7.8–100% of full aperture) were simulated. Note that the 64-element subaperture utilized the full aperture during transmit, and the sequence effectively averaged 15 diverging waves emitted from the same virtual source. Then, setting virtual sources to 15 and subaperture to 20 elements, angular apertures of 15° through 150° were simulated.

For steered compounding, angular aperture and tilt angle were investigated. Tilt was linearly spaced between the 15 virtual sources. For the remainder of the paper, tilt angle refers to the maximum absolute tilt of a transmission within a given sequence, denoting bounds within which the steering angle of each transmit is evenly spaced. While keeping the number of virtual sources at 15 and tilt angle at 20°, angular apertures of 15° through 150° were simulated. Then, setting the number of virtual sources at 15 and the angular aperture at 90°, tilt angles of 5° through 40° were simulated.

Strain accuracy of each of the above compounding sequences was evaluated by calculating the normalized strain error of axial $\left(\Delta\hat{\varepsilon}_{\text{axial}}\right)$, lateral $\left(\Delta\hat{\varepsilon}_{\text{lateral}}\right)$, and radial $\left(\Delta\hat{\varepsilon}_{\text{radial}}\right)$ cumulative strains. Noting that strain error could vary depending on the noise added to the RF signal to simulate decor-relation, five trials with unique randomized noise sets were generated to account for this variability. Scatterer distribution of the annulus and background, however, remained constant between sequences, and the same noise signals were added to the RF signals between the transmit configurations within the same trial.

C. Transthoracic imaging

Generally, increasing the number of virtual sources employed in coherent compounding has been shown to lead to improvement in sonographic SNR and strain estimation quality [16],

[29]. However, the number of virtual sources was set at the cost of frame rate: an increase in the number of transmits leads to a drop in the acquisition frame rate.

To determine the virtual source number and frame rate combination that leads to the most accurate strain estimation, a comparison study was performed with human subjects *in vivo*. All methods here were in compliance with the Institutional Review Board (IRB). Transthoracic parasternal short-axis views on the papillary muscle level were acquired from five self-reported healthy subjects (aged 25–35) by a trained research sonographer, in accordance with current echocardiography guidelines [38]. An ATL P4-2 phased array probe (20 mm aperture, 2.5 MHz center frequency, 0.320 mm pitch) connected to a research ultrasound system (Verasonics Vantage, Verasonics Redmond, WA) was used to image volunteers with a custom transmit sequence. Setting the PRF to 3000 Hz, five virtual sources and frame rate configurations were evaluated: 60 virtual sources at 50 Hz, 30 sources at 100 Hz, 15 sources at 200 Hz, 10 sources at 300 Hz, and 6 sourcesat 500 Hz. A custom sequence was designed such that each configuration would transmit following completion of the previous configuration's acquisition. Combining all five configurations within the same sequence ensured that any differences in myocardial mechanics between heart cycles were within the minimal, natural variation. Activation of the ultrasound sequence trigged the collection of ECG data, which was used to identify systole. For subaperture compounding, a 25-element subaperture and 90° angular aperture sequence for the five virtual source and frame rate configurations was implemented. For steered compounding, a 60° angular aperture and 15° tilt was used.

Beamforming, displacement estimation, and strain calculation was performed on the collected RF data as described previously. Prior to lateral displacement estimation, the acquisitions to be were downsampled to a frame rate of 100 Hz. Lateral displacements were then upsampled back to the original frame rate. For example, given the 500 Hz/6 transmit acquisition, the lateral displacement between every fifth frame was calculated. Linear temporal interpolation was then used to upsample the lateral displacement estimations back to 500 Hz to match the number of axial displacement frames. As explained in detail in the Discussion, the optimal lateral motion estimation rate is lower than that of the axial. Cumulative radial strains were estimated over the duration of systole, which was defined based on the ECG and assessment of M-mode visualization of the displacements. The mask was manually delineated based on assessment of the B-mode at end-diastole. The same mask was used for the strains estimated by the five configurations for a given subject. Sonographic SNR was calculated as the difference (in dB) between the mean B-mode magnitude within the masked region and the mean magnitude within the lumen, defined as the area within the endocardial border.

In order to quantitatively assess strain estimation precision, the Strain Filter was used [11], [39]. By calculating elastographic signal-to-noise ratio (SNR_e), the Strain Filter provides a means to estimate the degree of precision in a strain measurement, and allows for comparison between parameters sets. Briefly, SNR_e is defined as

$$SNR_e = \frac{\mu(\varepsilon)}{\sigma(\varepsilon)}. \quad (4)$$

SNR_e of radial strain within a 1.5 mm^2 window was calculated. The SNR_e window was translated throughout the masked area of radial strain. The resulting strain-SNR_e pairs were used to generate a 2D histogram representing the probability density function (pdf) of SNR_e. Normalizing for strain values that occur more frequently, the conditional pdf was expressed as $f(SNR_e|\varepsilon)$. The conditional pdf must be expressed as a 3D plot; for ease of comparison, the conditional expected value of the SNR_e may be calculated:

$$E(SNR_e|\varepsilon) = \int_0^{+\infty} SNR_e f(SNR_e|\varepsilon) dSNR_e \quad (5)$$

Previous applications of the Strain Filter were on interframe strains [11]. Here, it is used to evaluate end-systolic cumulative radial strains, prior to median filtering. SNR_e at approximately 41% radial strain was then statistically compared via a one- way ANOVA and Tukey-Kramer multiple comparison procedure. 41% strain was chosen because the peak SNR_e of the transmit configurations evaluated was approximately located at this strain value.

Once the frame rate configuration that yields the highest SNR_e for both transmit strategies was established, the two sequences were directly compared. For subaperture compounding, a 25-element subaperture (39% of full aperture) and 90° angular aperture sequence imaging at 300 Hz with 10 virtual sources was used. For steered compounding, a 60° angular aperture and 15° tilt sequence imaging at 300 Hz with 10 virtual sources was used. The compounding sequences were combined into a custom sequence, wherein a steered compounding acquisition would immediately follow a subaperture compounding acquisition. Five self-reported healthy subjects (aged 25–30) were transthoracically imaged at the parasternal short axis view. Displacements and strains were calculated as previously described. The Strain Filter was implemented to quantitatively assess the precision of the strain estimation of each sequence. Statistical comparison between the SNR_e of the two compounding types at 41% cumulative strain was performed using a paired t-test. 41% strain was chosen because the peak SNR_e of the transmit configurations evaluated was approximately located at this strain value.

III. Results

A. Analysis of simulation

Fig. 4 summarizes the simulation results for the subaperture compounding optimization. Strain estimation accuracy as a function of subaperture is summarized in Fig. 4a. A 25-element subaperture yielded the most accurate strain estimation ($\Delta\hat{\varepsilon}_{\text{lateral}} = 42.5\%$, $\Delta\hat{\varepsilon}_{\text{axial}} = 22.2\%$, $\Delta\hat{\varepsilon}_{\text{radial}} = 27.5\%$). Using the Tukey-Kramer method, the 25 element subaperture estimated lateral and radial strain with less error than a subaperture with 5–15

elements and 45–64 elements ($p<0.05$). There was no significant difference between a subaperture of 25 and 35 in estimating the three types of cumulative strains; however, a subaperture of 25 elements was significantly different with a greater number of subaperture configurations compared to 35 elements. There was no significant difference between the axial strain estimation accuracy of the 25 element subaperture with the other subaperture configurations.

Strain estimation accuracy as a function of angular aperture in simulation is summarized in Fig. 4b. A 90° angular aperture yields the lowest total normalized squared error ($\Delta\hat{\varepsilon}_{\text{lateral}} = 41.3\%$, $\Delta\hat{\varepsilon}_{\text{axial}} = 21.6\%$, $\Delta\hat{\varepsilon}_{\text{radial}} = 28.3\%$). Laterally, a 90° angular aperture yielded less estimation error statistically compared with angular apertures of 15° and 105°–150° ($p<0.05$). Axially, strain was estimated more accurately at 90° than at 120° and 150° ($p<0.05$). Radially, strain estimation was more accurate at 90° than at 15° and 120°–150° ($p<0.05$).

Fig. 5 summarizes the simulation results for the steered compounding optimization. Strain estimation accuracy as a function of angular aperture is summarized in Fig. 5a. The best angular apertures for steered compounding were 45°, 60°, and 75° (for 45°: $\Delta\hat{\varepsilon}_{\text{lateral}} = 31.1\%$, $\Delta\hat{\varepsilon}_{\text{axial}} = 19.8\%$, $\Delta\hat{\varepsilon}_{\text{radial}} = 24.2\%$; for 60°: $\Delta\hat{\varepsilon}_{\text{lateral}} = 31.2\%$, $\Delta\hat{\varepsilon}_{\text{axial}} = 19.5\%$, $\Delta\hat{\varepsilon}_{\text{radial}} = 23.9\%$; for 75°: $\Delta\hat{\varepsilon}_{\text{lateral}} = 33.4\%$, $\Delta\hat{\varepsilon}_{\text{axial}} = 20.0\%$, $\Delta\hat{\varepsilon}_{\text{radial}} = 24.4\%$). Statistically, the three angular aperture configurations were equivalently accurate for axial, lateral, and radial strain. Laterally, strain estimation was more accurate at 45–75° than at 15°–30° and 120°–150° ($p<0.05$). Axially, superior accuracy was achieved at 45–75° than at 15° and 90°–150° ($p<0.05$). For radial strain estimation, estimation error was lower at 45–75° than at 15°–30° and 120°–150° ($p<0.05$).

Strain estimation accuracy was investigated as a function of tilt angle in steered compounding; results are shown in Fig. 5b. A tilt angle of 15° was determined to yield the most accurate strain estimation in general ($\Delta\hat{\varepsilon}_{\text{lateral}} = 33.1\%$, $\Delta\hat{\varepsilon}_{\text{axial}} = 21.0\%$, $\Delta\hat{\varepsilon}_{\text{radial}} = 24.1\%$); For lateral strain estimation, error was significantly lower at 15° compared to tilt angles of 5°–10° and 25°–40° ($p<0.05$). Axially, strain was estimated more accurately at 15° compared to the tilt angle of 40° ($p<0.05$). Radially, estimation accuracy was superior at 15° than at 5°–10° and 25°–40° ($p<0.05$).

B. Analysis of steered and subaperture compounding in transthoracic imaging

Fig. 6 summarizes the cumulative radial strains obtained from subaperture compounding. Given that the subjects being imaged are had normal cardiac function, the radial strain should exhibit uniformly positive strain throughout the masked region. The strains estimated by the frame rate configurations of 100 Hz/30 sources, 200 Hz/15 sources, 300 Hz/10 sources, and 500 Hz/6 sources are as expected: strain is generally homogeneously positive. In contrast, the frame rate configuration of 50 Hz/60 sources produced a radial strain estimate that is less homogenously positive. The anterior region is primarily characterized as an area of low strain; this is in sharp contrast with the assessment of the other frame rate configurations, which identify the area primarily as a positive high strain region.

Furthermore, the magnitude of the posterior strain of the 50 Hz configuration is markedly low, in direct contrast to the results from the other frame rate configurations which identify the region as an area of high magnitude positive strain.

Fig. 7 summarizes the radial cumulative strains from steered compounding imaging. Strains estimated by the frame rate configurations of 200 Hz/15 sources, 300 Hz/10 sources, and 500 Hz/6 sources are qualitatively virtually identical, exhibiting homogenous positive strain throughout the myocardium. In contrast, the radial strain estimated by the 100 Hz/30 sources and 50 Hz/60 sources configuration is characterized by significant areas of low or zero strain regions in the anterior and posterior, which would erroneously indicate the presence of ischemia in the myocardium of a healthy subject.

Strain estimation precision was assessed using the Strain Filter. The $E(SNR_e|\varepsilon)$ curves of the five frame rate configurations for subaperture compounding are shown in Fig. 8. Overall, the cumulative end-systolic radial strains estimated by frame rate configurations of 500 Hz/6 sources, 300 Hz/10 sources, and 200 Hz/15 sources have higher $E(SNR_e|\varepsilon)$ across the strain range of interest compared to the 100 Hz/30 sources and 50 Hz/60 sources sequences. In order to validate that significant differences in $E(SNR_e|\varepsilon)$ were present between the different frame rate configurations, the $E(SNR_e|\varepsilon)$ values of each frame rate configuration at 41% strain across the five subjects was statistically evaluated using a one-way ANOVA and Tukey-Kramer multiple comparison tests. 41% strain was chosen since the $E(SNR_e|\varepsilon)$ of all five configurations peak at approximately that strain value. It was determined that a configuration of 300 Hz ($E(SNR_e|\varepsilon = 41\%) = 4.28$) estimated strains more precisely than the 50 Hz configuration ($E(SNR_e|\varepsilon = 41\%) = 2.16$) with great statistical certainty ($p<0.01$). 500 Hz also estimated strains at 41% more precisely ($E(SNR_e|\varepsilon = 41\%) = 3.85$), albeit at a lower significance level ($p<0.05$). There was no statistically significant difference between the 100–200 Hz and 50 Hz configurations in subaperture compounding.

The Strain Filter was also used to evaluate how different frame rate configurations in steered compounding would affect radial strain estimation precision, summarized in Fig. 9. The $E(SNR_e|\varepsilon)$ curves generated by steered compounding are similar to those calculated by subaperture compounding: 500 Hz/6 sources, 300 Hz/10 sources, and 200 Hz/15 sources are more precise across the strain range of interest compared to the 100 Hz/30 transmits and 50 Hz/60 transmits sequences. Likewise, as determined in the subaperture compounding analysis, the one-way ANOVA and Tukey Kramer multiple comparison tests indicated that there was a significant difference in strain estimation precision between 50 Hz ($E(SNR_e|\varepsilon = 41\%) = 2.41$) and 300 Hz ($E(SNR_e|\varepsilon = 41\%) = 4.03$) ($P<0.01$). At a lower statistical significance level ($p<0.05$), the 500 Hz configuration ($E(SNR_e|\varepsilon = 0.41) = 3.58$) was also found to measure strain more precisely compared to the 50 Hz configuration. As with subaperture compounding, there was no statistically significant difference in strain estimation precision between the 100–200 Hz and 50 Hz configurations in steered compounding.

Once the best parameter configuration for subaperture compounding (25 element subaperture, 90° angular aperture, 300 Hz/10 sources) and steered compounding (25 element subaperture, 90° angular aperture, 300 Hz/10 sources) was determined, the two types of

compounding sequences were directly compared. Fig. 10 summarizes the results of this comparison. The end-systolic radial strains are shown in Fig. 10a-b. Qualitatively, the radial strains produced by both methods were nearly identical. Quantitative assessment of the radial strains was performed with the Strain Filter; results are summarized in Fig. 10c. Between the strain range of 30% and 50%, the subaperture $E(SNR_e|\varepsilon)$ is higher compared to its steered counterpart. However, statistical comparison of $E(SNR_e|\varepsilon)$ at 41% strain, at which point strain precision for steered compounding ($E(SNR_e|\varepsilon = 0.41) = 3.56$) and subaperture compounding ($E(SNR_e|\varepsilon = 0.41) = 4.26$) peaks, indicates that there is no significant difference in the $E(SNR_e|\varepsilon = 0.41)$ obtained by the two techniques (Fig. 9d, $p = 0.46$).

IV. Discussion

The objectives of this study were to determine the optimal transmit parameters for subaperture and steered compounding for Myocardial Elastography. Once these parameters were determined, the two compounding methods could be directly compared *in vivo*. Via simulation it was determined that sub-aperture compounding yields the most accurate strains when a subaperture of 25 elements (39% of full aperture) and angular aperture of 90° is employed. For steered compounding, an angular aperture of 60° and tilt of 15° was determined to be the best parameters. In transthoracic imaging of healthy subjects, it was determined that the most precise strain estimation was achieved at 300 Hz/10 sources, and that there was no significant difference in strain estimation precision between the two compounding approaches.

The tradeoffs inherent in the transmit parameters selected in this study are evident upon inspection of the simulation results (Fig. 4 and 5). Throughout, the minima of estimation error lies between the extreme settings of a given parameter, which reflect the physics underlying each transmit parameter. The size of the subaperture in subaperture compounding dictates lateral resolution and pressure output. The advantage of having a large virtual aperture is that lateral resolution is enhanced (Fig. 2a) [16], [24]. However, the tradeoff is decreased pressure output (Fig. 3a), which will lead to a subsequent drop in SNR. A subaperture of 25 elements solves the tradeoff between virtual aperture size and sufficient pressure output. Similarly, angular aperture for both subaperture (Fig. 2b) and steered (Fig. 3a) compounding requires tradeoffs to be balanced. A smaller angular aperture yields increased transmitted pressure (Fig. 2b–c), whereas a larger angular aperture allows for superior resolution (Fig. 3b–c) and greater field-of-view. Angular apertures of 90° and 45–75° for subaperture and steered compounding, respectively, was shown to estimate strain with the least error. It was anticipated that the angular aperture for steered compounding would be narrower than that of subaperture compounding, since the diverging waves of the former are steered, such that the center of the field-of-view is sufficiently insonified. In regards to the tilt angle in steered compounding, it was shown that 15° yielded the most accurate estimation (Fig 5b). Increasing tilt yields improvements in resolution (Fig. 2d), at the cost of reduced transmit pressure (Fig. 3d). A tilt of 15° ensures that both high resolution and sufficient transmit pressure is achieved.

The number of virtual sources was investigated via transthoracic imaging of healthy human subjects. Like the transmit parameters discussed above, the number of virtual sources has

tradeoffs that must be considered. SNR is critical in echocardiographic applications, and increasing the number of virtual sources generally leads to an improvement in strain estimation quality [16], [24], [29], [30]. The average sonographic SNR of the evaluated transmit configurations is summarized in Table I, and corroborates this finding. However, increasing the number of transmits leads to a reduction in the frame rate. Although perhaps less critical for sonographic quality, a sufficiently high motion estimation rate is of utmost importance for accurate and precise strain estimation when using normalized cross-correlation on RF signals, since both phase and envelope information are used [11]. ME estimates radial strain by first estimating the displacement in the axial and lateral directions. At sufficiently high motion estimation rates, accurate axial displacement estimation may be achieved; in previous publications, our group has shown that a single diverging wave sequence at 2000 Hz can image small incremental axial strains ($\varepsilon < 0.025\%$) associated with the electromechanical coupling in the *in vivo* myocardium with high reproducibility [40].

In contrast, the results demonstrated here indicate that the lateral displacement estimation is less reliant on a high motion estimation rate compared to the axial estimator [11]. Indeed, a lower motion estimation rate is preferred. Fig. 11 compares the radial strain estimation with and without lateral downsampling. In comparing the lateral strain estimated by the 500 Hz sequence without lateral motion estimation rate downsampling (Fig. 11c) to the strain estimated with lateral displacement downsampled to 100 Hz (Fig. 11a), it is clear that the latter leads to more physiologically accurate outcome. Notably, the lateral strain estimate without downsampling reflects large negative strain regions in the endocardial portion of the lateral wall (Fig. 11a), which is an erroneous feature absent from the estimate with downsampling (Fig. 11b). The poor lateral strain estimation leads to artifacts that arise in the radial strain (Fig. 11c) that are absent in the radial when the lateral estimate is downsampled (Fig. 11d); note the negative strain region in the antero-lateral, indicative of ischemia or infarct or dyssynchrony in the LV contraction pattern. The lateral estimation, which is limited by relatively coarse sampling, may benefit from a low motion estimation rate because it allows for significant amount of lateral motion to occur. This is consistent with previous reports that concluded that while axial strain estimator is sensitive to small strains, the lateral strain estimator specializes in measuring large magnitude strains irrespective of frame rate [11], [41]. Improving SNR and spatial resolution is therefore the preferred approach to increasing the accuracy and precision of lateral displacement and strain estimation, since the effect of motion estimation rate is limited. When selecting the number of transmits to incorporate into the sequence, it is thus necessary to balance the need for superior SNR and high frame rate, and the needs of axial versus lateral displacement and strain estimation.

The relationship between axial and lateral estimation with SNR and frame rate is evident upon close examination of the radial strains acquired from the healthy subjects. For both subaperture and steered compounding, the 50 Hz frame rate configuration yielded less qualitatively accurate strains and poorer precision compared to acquisitions at other frame rates. The areas of poor or incorrect strain estimation were generally in the anterior and posterior regions of the myocardium, areas that rely heavily on accurate axial strain estimation (Fig. 6A and 7A). Precise axial displacement estimation cannot occur at such low frame rates, and the resulting decorrelation lead to inaccurate radial strains. Note that the

lateral and septal regions of the radial strains estimated by the 50 Hz configuration, in contrast, more closely resemble their higher frame rate counterparts (Fig. 6 and 7).

In the absence of a true strain value, the Strain Filter was used to establish the performance of the sequences evaluated in this paper. The validity of the SNR_e metric is founded on the assumption that the myocardial strain within a small window (1.5 mm^2) should be fairly constant. As shown in the definition of SNR_e (Eq. 8), variations in strain within that window lead to a decreased SNR_e, which is indicative of decorrelation in the estimator. The Strain Filter is thus an excellent metric for measuring the precision of the estimator. However, it is an imperfect tool. Abnormally high strains caused by decorrelation may erroneously contribute to a high SNR_e value. Furthermore, the Strain Filter cannot assess whether the spatial strain distribution is correct, i.e. it cannot measure accuracy. It is therefore imperative that the Strain Filter be used in conjunction with qualitative analysis of the estimated strains and strain images, to ensure that the spatial distribution and direction of the strains is appropriate. Radial strain was used to evaluate the compounding sequences in transthoracic imaging given that it is expected to be uniformly positive, which simplifies qualitative verification of the Strain Filter metric, and because it assesses the precision of both radial and lateral displacement and strain estimation.

Transthoracic imaging of the five healthy subjects as described here indicates that the compounding methods provide equivalent performance. However, it should be noted that patients who undergo echocardiography to screen for ischemia or infarction are on average of more advanced BMI and age, or have other pathologies that render transthoracic imaging more challenging. It is possible that the increased pressure output allowed by steered compounding may offer an advantage in this specific patient population. Note that the transmit voltage could not be increased in partial aperture subaperture compounding to match the pressure output of full aperture steered compounding. Characterization of the probe had indicated the transmit voltage may be maximized for a full aperture, 64-element transmit without exceeding the MI and ISPTA limits mandated by the FDA for human echocardiography. Consequently, hardware limitations (i.e. further increase in transmit voltage would risk probe damage) precluded increasing power per element in subaperture configurations.

Optimization of the radial and circumferential strain estimation in the short-axis view was the primary objective of this paper. The short axis view allows for simultaneous visualization of myocardial tissue perfused by the three main coronary arteries (left anterior descending, left circumflex, right coronary), which is ideal for ischemia and infarct localization. Acquisition of longitudinal strain in the apical view likewise has significant clinical value. While this study has some relevance to longitudinal strain imaging, given that it is reliant on axial displacement estimation which is investigated here, the differences in myocardium mechanics in the short versus apical views may lead to a different set of optimal parameters that would necessitate a future study to elucidate.

This paper aimed to determine the transmit parameters in compounding that yielded the most accurate and precise strain estimation. There are several other variables in the strain estimation pipeline that may lead to more accurate measurements that are beyond the scope

of this paper. Optimization and comparison of compounding strategies was performed with a ATL P4-2; a different configuration of a phased array employing a different bandwidth or pitch may have distinct optimal parameters that vary slightly compared the specifications recommended here. A delay-and-sum beamformer was used here; implementation of alternative beamforming schemes, such as Capon, may lead to superior speckle resolution and consequently higher strain estimation accuracy and precision [42]. For lower frame rate configurations with a large number of virtual sources, significant displacement between subsequent transmits may occur, leading to decorrelation; a number of motion compensation methods exist that could be implemented, and may improve upon the strain accuracy and precision of some of the sequences discussed here [15], [26], [43]–[45]. This effect may also explain why the 60 sources configurations produces inferior sonographic SNR compared to the 30 sources configuration (Table I). Finally, aberrations and reverberations caused by peripheral organs were not simulated in Field II.

V. Conclusion

The transmit parameters for compounding using partial and full transmit apertures was investigated as it pertains to the cardiac strain estimation quality. For subaperture compounding, it was concluded that a 25-element subaperture (39% of full aperture) and 90° angular aperture estimates axial, lateral, and radial strain most accurately in simulations; for steered compounding, an angular aperture within 45°–75° and tilt angle of 15° was found to be optimal. Transthoracic imaging indicated that both compounding approaches estimated strain at 300 Hz/10 sources with the highest qualitative accuracy and precision. Finally, directly comparing the optimized sub-aperture compounding sequence with the optimized steered compounding sequence in transthoracic imaging of healthy subjects indicated that there was no significant difference in the strain estimation accuracy or precision.

Acknowledgments

This study was supported in part by the National Institutes of Health (EB006042) and the W.H. Coulter Foundation.

The authors thank Eric J. Stöhr, PhD (Discipline of Medicine, Division of Cardiology, Columbia University Irving Medical Center, New York City, NY 10032, USA; School of Health Sciences, Cardiff Metropolitan University, Cardiff, UK) for image acquisition.

Appendix

A. Beamforming and coherent compounding

Reconstruction of RF signals was performed with a delay-and-sum beamformer. The polar reconstruction grid featured a 90° field-of-view with 180 lines and 20 MHz axial sampling. Time of flight, T, between time of transmit ($T_{forward}$) from the array, and time of receive ($T_{backward}$) was defined as

$$T = T_{forward} + T_{backward} + T_{delay}. \quad (6)$$

Transmission time of flight $T_{forward}$ is defined as follows,

$$T_{forward} = \frac{\sqrt{(x - x_{vs})^2 + (z - z_{vs})^2}}{c}, \quad (7)$$

where x and z are the Cartesian lateral and axial coordinates of the points of the reconstruction grid, respectively, and c is speed of sound, assumed to be 1540 m/s. Receive time of flight was defined as follows:

$$T_{backward} = \frac{\sqrt{(x - e_i)^2 + z^2}}{c}, \quad (8)$$

where e_i is the lateral position of the element. All elements were used during receive. Finally, T_{delay}, which accounts for the virtual propagation time between the virtual source and the aperture, is defined as

$$T_{delay} = \frac{z_{vs}}{c}. \quad (9)$$

The resulting beamformed RF signals are subsequently summed over the number of transmits to generate a coherently compounded RF data set that can be processed for displacement estimation.

References

1. Abraham TP, Dimaano VL, Liang H-Y. Role of tissue Doppler and strain echocardiography in current clinical practice. Circulation. Nov; 2007 116(22):2597–2609. [PubMed: 18040039]
2. D'hooge J, et al. Regional Strain and Strain Rate Measurements by Cardiac Ultrasound: Principles, Implementation and Limitations. Eur Heart J - Cardiovasc Imaging. Sep; 2000 1(3):154–170.
3. Smiseth OA, Torp H, Opdahl A, Haugaa KH, Urheim S. Myocardial strain imaging: how useful is it in clinical decision making? Eur Heart J. Apr; 2016 37(15):1196–1207. [PubMed: 26508168]
4. Dandel M, Lehmkuhl H, Knosalla C, Suramelashvili N, Hetzer R. Strain and Strain Rate Imaging by Echocardiography – Basic Concepts and Clinical Applicability. Curr Cardiol Rev. May; 2009 5(2): 133–148. [PubMed: 20436854]
5. Konofagou EE, D'hooge J, Ophir J. Myocardial elastography— a feasibility study in vivo. Ultrasound Med Biol. Apr; 2002 28(4):475–482. [PubMed: 12049961]
6. Lee W-N, Ingrassia CM, Fung-Kee-Fung SD, Costa KD, Holmes JW, Konofagou EE. Theoretical Quality Assessment of Myocardial Elastography with In Vivo Validation. IEEE Trans Ultrason Ferroelectr Freq Control. 2007; 54(11):2233–2245. [PubMed: 18051158]
7. Luo J, Fujikura K, Homma S, Konofagou EE. Myocardial Elastography at Both High Temporal and Spatial Resolution for the Detection of Infarcts. Ultrasound Med Biol. Aug; 2007 33(8):1206–1223. [PubMed: 17570577]
8. Lee W-N, Provost J, Fujikura K, Wang J, Konofagou EE. In vivo study of myocardial elastography under graded ischemia conditions. Phys Med Biol. Feb.2011 56(4):1155. [PubMed: 21285479]
9. Grondin J, Wan E, Gambhir A, Garan H, Konofagou E. Intrac-ardiac myocardial elastography in canines and humans in vivo. IEEE Trans Ultrason Ferroelectr Freq Control. Feb; 2015 62(2):337–349. [PubMed: 25643083]

10. Grondin J, Waase M, Gambhir A, Bunting E, Sayseng V, Konofagou EE. Evaluation of Coronary Artery Disease Using Myocardial Elastography with Diverging Wave Imaging: Validation against Myocardial Perfusion Imaging and Coronary Angiography. Ultrasound Med Biol. May; 2017 43(5):893–902. [PubMed: 28256343]
11. Bunting EA, Provost J, Konofagou EE. Stochastic precision analysis of 2D cardiac strain estimation in vivo. Phys Med Biol. Nov; 2014 59(22):6841–6858. [PubMed: 25330746]
12. Chen H, Varghese T, Rahko PS, Zagzebski JA. Ultrasound frame rate requirements for cardiac elastography: Experimental and in vivo results. Ultrasonics. Jan; 2009 49(1):98–111. [PubMed: 18657839]
13. Wang S, Lee W-N, Provost J, Luo J, Konofagou EE. A composite high-frame-rate system for clinical cardiovascular imaging. IEEE Trans Ultrason Ferroelectr Freq Control. Oct; 2008 55(10): 2221–2233. [PubMed: 18986870]
14. Holländer B, Hendriks GAGM, Mann RM, Hansen HHG, Korte CLde. Plane-Wave Compounding in Automated Breast Volume Scanning: A Phantom-Based Study. Ultrasound Med Biol. Jul.2016
15. Montaldo G, Tanter M, Bercoff J, Benech N, Fink M. Coherent plane-wave compounding for very high frame rate ultrasonography and transient elastography. IEEE Trans Ultrason Ferroelectr Freq Control. Mar; 2009 56(3):489–506. [PubMed: 19411209]
16. Papadacci C, Pernot M, Couade M, Fink M, Tanter M. High-contrast ultrafast imaging of the heart. IEEE Trans Ultrason Ferroelectr Freq Control. Feb; 2014 61(2):288–301. [PubMed: 24474135]
17. Nayak R, et al. Principal Strain Vascular Elastography: Simulation and Preliminary Clinical Evaluation. Ultrasound Med Biol. Mar; 2017 43(3):682–699. [PubMed: 28057387]
18. Porée J, Garcia D, Chayer B, Ohayon J, Cloutier G. Noninvasive Vascular Elastography With Plane Strain Incompressibility Assumption Using Ultrafast Coherent Compound Plane Wave Imaging. IEEE Trans Med Imaging. Dec; 2015 34(12):2618–2631. [PubMed: 26625341]
19. Korukonda S, Nayak R, Carson N, Schifitto G, Dogra V, Doyley MM. Noninvasive vascular elastography using plane-wave and sparse-array imaging. IEEE Trans Ultrason Ferroelectr Freq Control. Feb; 2013 60(2):332–342. [PubMed: 23357907]
20. Denarie B, et al. Coherent Plane Wave Compounding for Very High Frame Rate Ultrasonography of Rapidly Moving Targets. IEEE Trans Med Imaging. Jul; 2013 32(7):1265–1276. [PubMed: 23549887]
21. Apostolakis IZ, McGarry MDJ, Bunting EA, Konofagou EE. Pulse wave imaging using coherent compounding in a phantom and in vivo. Phys Med Biol. 2017; 62(5):1700. [PubMed: 28002039]
22. Hansen HHG, Saris AECM, Vaka NR, Nillesen MM, de Korte CL. Ultrafast vascular strain compounding using plane wave transmission. J Biomech. Mar; 2014 47(4):815–823. [PubMed: 24484646]
23. Correia M, Provost J, Chatelin S, Villemain O, Tanter M, Pernot M. Ultrafast Harmonic Coherent Compound (UHCC) Imaging for High Frame Rate Echocardiography and Shear-Wave Elastography. IEEE Trans Ultrason Ferroelectr Freq Control. Mar; 2016 63(3):420–431. [PubMed: 26890730]
24. Sayseng V, Grondin J, Papadacci C, Costet A, Konofagou E. Optimization of transmit parameters for two-dimensional cardiac strain estimation with coherent compounding in silico, in vitro, and in vivo. 2016 IEEE International Ultrasonics Symposium (IUS). 2016:1–4.
25. Nillesen MM, et al. Cardiac Motion Estimation Using Ultrafast Ultrasound Imaging Tested in a Finite Element Model of Cardiac Mechanics. Functional Imaging and Modeling of the Heart. 2015:207–214.
26. Poree J, Posada D, Hodzic A, Tournoux F, Cloutier G, Garcia D. High-Frame-Rate Echocardiography Using Coherent Compounding With Doppler-Based Motion-Compensation. IEEE Trans Med Imaging. Jul; 2016 35(7):1647–1657. [PubMed: 26863650]
27. Zhao F, Tong L, He Q, Luo J. Coded excitation for diverging wave cardiac imaging: a feasibility study. Phys Med Biol. 2017; 62(4):1565. [PubMed: 28076337]
28. Hasegawa H, Kanai H. High-frame-rate echocardiography using diverging transmit beams and parallel receive beamforming. J Med Ultrason. Jul; 2011 38(3):129–140.

29. Grondin J, Sayseng V, Konofagou EE. Cardiac Strain Imaging With Coherent Compounding of Diverging Waves. IEEE Trans Ultrason Ferroelectr Freq Control. Aug; 2017 64(8):1212–1222. [PubMed: 28644803]
30. Nayak R, Schifitto G, Doyley MM. Noninvasive carotid artery elastography using multielement synthetic aperture imaging: Phantom and in vivo evaluation. Med Phys. Aug; 2017 44(8):4068–4082. [PubMed: 28494102]
31. Jensen JA. FIELD: A Program for Simulating Ultrasound Systems. 10th Nordicbaltic Conference on Biomedical Imaging, Vol 4, Supplement 1, Part 1:351–353. 1996:351–353.
32. Culjat MO, Goldenberg D, Tewari P, Singh RS. A Review of Tissue Substitutes for Ultrasound Imaging. Ultrasound Med Biol. Jun; 2010 36(6):861–873. [PubMed: 20510184]
33. Lang RM, et al. Recommendations for chamber quantification. Eur J Echocardiogr. Mar; 2006 7(2):79–108. [PubMed: 16458610]
34. Carlsson M, Ugander M, Mosén H, Buhre T, Arheden H. Atrioventricular plane displacement is the major contributor to left ventricular pumping in healthy adults, athletes, and patients with dilated cardiomyopathy. Am J Physiol - Heart Circ Physiol. Mar; 2007 292(3):H1452–H1459. [PubMed: 17098822]
35. Buchalter MB, et al. Noninvasive quantification of left ventricular rotational deformation in normal humans using magnetic resonance imaging myocardial tagging. Circulation. Apr; 1990 81(4): 1236–1244. [PubMed: 2317906]
36. Kim H-K, et al. Assessment of Left Ventricular Rotation and Torsion with Two-dimensional Speckle Tracking Echocardiography. J Am Soc Echocardiogr. Jan; 2007 20(1):45–53. [PubMed: 17218201]
37. Kallel F, Ophir J. A Least-Squares Strain Estimator for Elastography. Ultrason Imaging. Jul; 1997 19(3):195–208. [PubMed: 9447668]
38. Lang RM, et al. Recommendations for Cardiac Chamber Quantification by Echocardiography in Adults: An Update from the American Society of Echocardiography and the European Association of Cardiovascular Imaging. J Am Soc Echocardiogr. Jan; 2015 28(1):1–39.e14. [PubMed: 25559473]
39. Varghese T, Ophir J. A theoretical framework for performance characterization of elastography: the strain filter. IEEE Trans Ultrason Ferroelectr Freq Control. Jan; 1997 44(1):164–172. [PubMed: 18244114]
40. Melki L, Costet A, Konofagou EE. Reproducibility and Angle Independence of Electromechanical Wave Imaging for the Measurement of Electromechanical Activation during Sinus Rhythm in Healthy Humans. Ultrasound Med Biol. Aug.2017
41. Lee, W-N. Myocardial Elastography: A Strain Imaging Technique for the Reliable Detection and Localization of Myocardial Ischemia in Vivo. Columbia University; New York, NY, USA: 2010.
42. Wang Z, Li J, Wu R. Time-delay- and time-reversal-based robust capon beamformers for ultrasound imaging. IEEE Trans Med Imaging. Oct; 2005 24(10):1308–1322. [PubMed: 16229417]
43. Trahey GE, Nock LF. Synthetic receive aperture imaging with phase correction for motion and for tissue inhomogeneities. II. Effects of and correction for motion. IEEE Trans Ultrason Ferroelectr Freq Control. Jul; 1992 39(4):496–501. [PubMed: 18267661]
44. Kim KS, Hwang JS, Jeong JS, Song TK. An efficient motion estimation and compensation method for ultrasound synthetic aperture imaging. Ultrason Imaging. Apr; 2002 24(2):81–99. [PubMed: 12199420]
45. Gammelmark KL, Jensen JA. 2-D tissue motion compensation of synthetic transmit aperture images. IEEE Trans Ultrason Ferroelectr Freq Control. Apr; 2014 61(4):594–610.

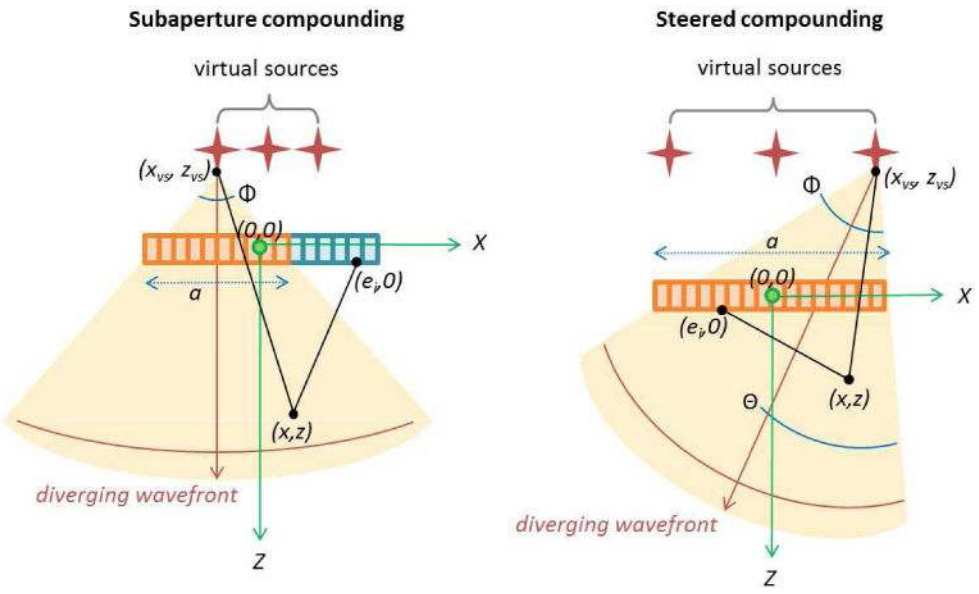

Fig. 1.

Illustration of critical parameters and beamforming variables in subaperture and steered compounding with three virtual sources. Virtual sources dictate the number of diverging waves transmitted, and are represented as four-point red stars. Elements activated during transmit are denoted as orange, while inactive elements are identified as blue. In subaperture compounding, only a portion of the aperture—the subaperture, a—is used in transmit. The angular aperture Φ is the angle created by the vectors between the virtual source and the ends of the subaperture. A constraint of subaperture compounding is that the virtual source must be placed at the center of the subaperture, thus generating a non-steered diverging wave. In steered compounding, this constraint is not implemented, and the full aperture is always used in transmit. This results in a steered diverging wave; the degree of steer is defined by the tilt angle, Θ.

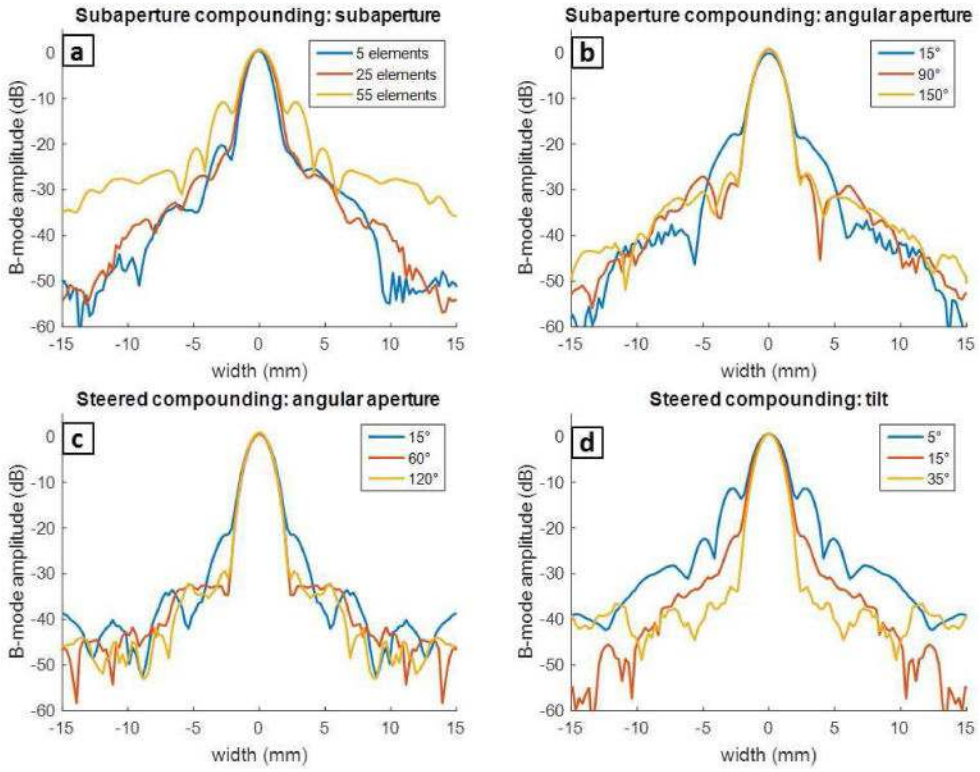

Fig. 2.

PSFs of compounding transmit configurations at 60 mm depth as a function of subaperture (a) and angular aperture (b) in subaperture compounding, and angular aperture (c) and tilt (d) in steered compounding. All transmit configurations implemented 15 virtual sources.

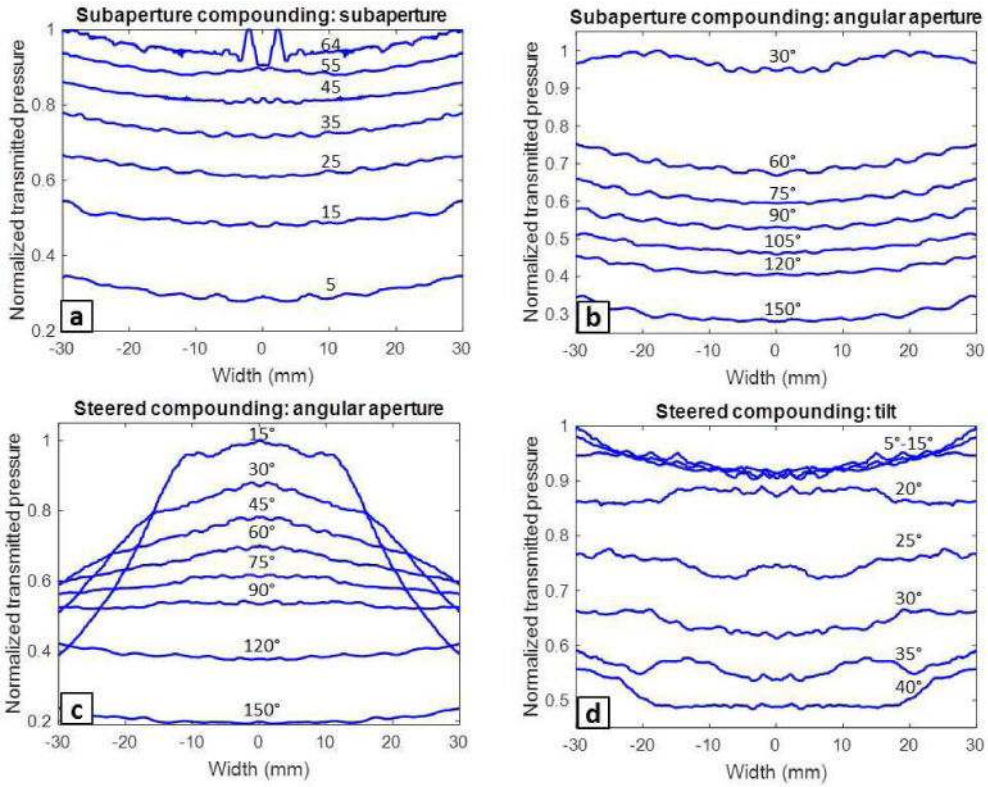

Fig. 3.

Normalized transmitted pressure at 60 mm depth as a function of subaperture (a) and angular aperture (b) in subaperture compounding, and angular aperture (c) and tilt (d) in steered compounding. All transmit configurations implemented 15 virtual sources. Figure 9. Strain estimation accuracy of steered compounding in transthoracic imaging of five healthy subjects was determined with the strain filter. The average $E(SNRe|\varepsilon)$ over five subjects as a function of strain from 1% to 100% strain is shown (a). The expected SNRe of each frame rate configuration at 41% strain (denoted by brown dashed line), at approximately which the strain estimator yields the most accurate strains, was statistically compared with a one-way ANOVA and Tukey-Kramer multiple comparison test (b). The 500 Hz configuration is significantly more accurate compared to 50 Hz ($p<0.05$); the 300 Hz configuration is likewise more accurate compared to 50 Hz, but at a higher significance level ($p<0.01$).

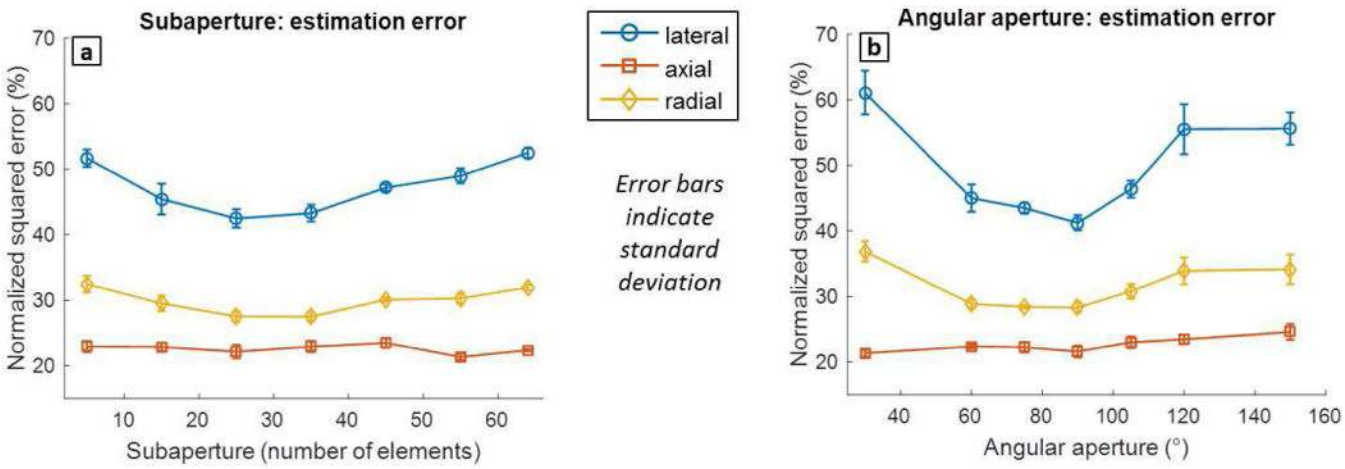

Fig. 4.

Investigation into transmit parameters of subaperture compounding in simulation. Cumulative axial, lateral and radial strain estimation accuracy are determined by calculating normalized square error as a function of subaperture (a) and angular aperture (b). Errorbars indicate standard deviation. A subaperture of 25 and angular aperture of 90° yielded the lowest estimation errors, and were used in the transthoracic imaging sequence.

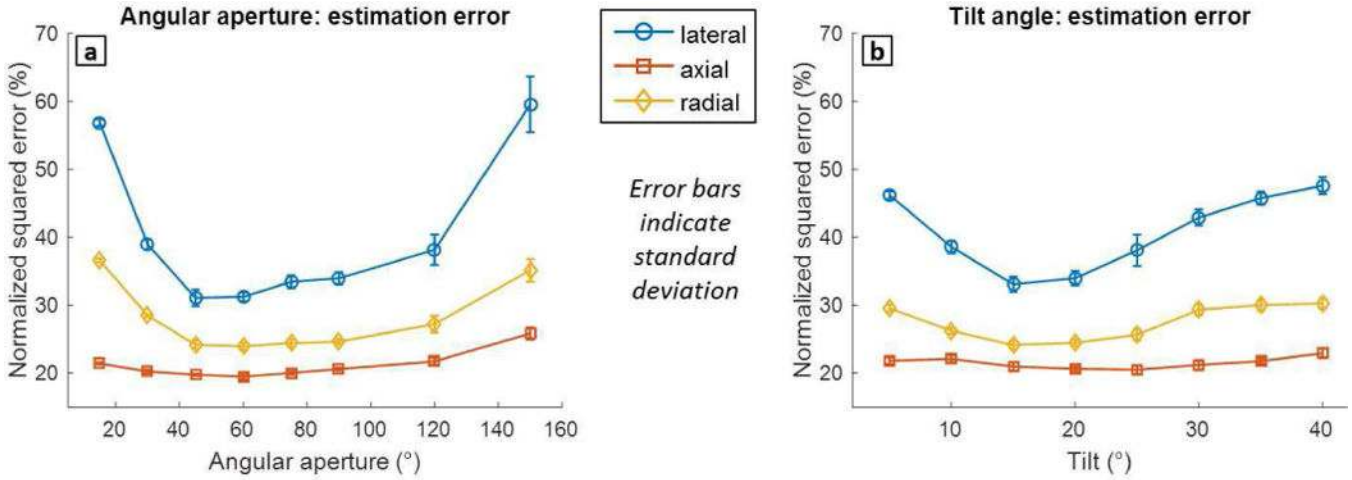

Fig. 5.

Investigation into transmit parameters of steered compounding in simulation. Cumulative axial, lateral and radial strain estimation accuracy are determined by calculating normalized square error as a function of angular aperture (a) and tilt angle (b). Errorbars indicate standard deviation. An angular aperture of 60° and tilt angle of 15° yielded the lowest estimation errors, and were used in the transthoracic imaging sequence.

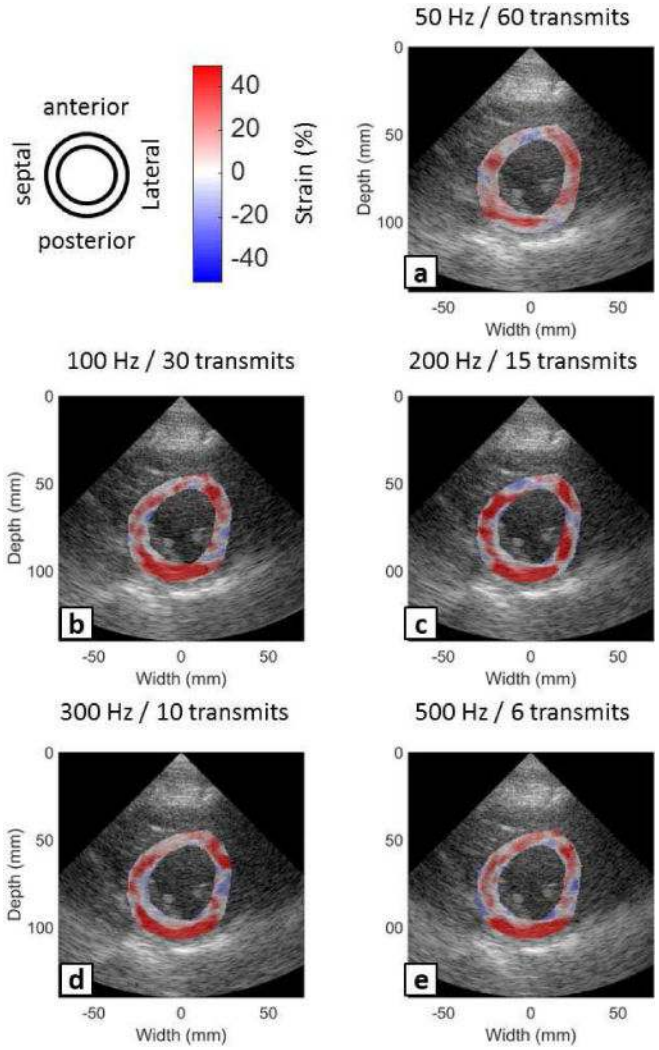

Fig. 6.

Left ventricular cumulative radial strains acquired via transthoracic imaging with subaperture compounding at 3000 PRF. Five frame rate/transmit number configurations were investigated. As the subject was healthy, it was expected that the transthoracic parasternal short axis view should yield homogenously positive strain. Strain estimated with frame rate configurations of 100 Hz to 500 Hz (b–e) are similar, indicating good myocardial health as anticipated. In contrast, the 50 Hz configuration (a) shows areas of zero and low magnitude strain in the anterior and posterior, erroneously suggesting ischemia in those areas of the heart.

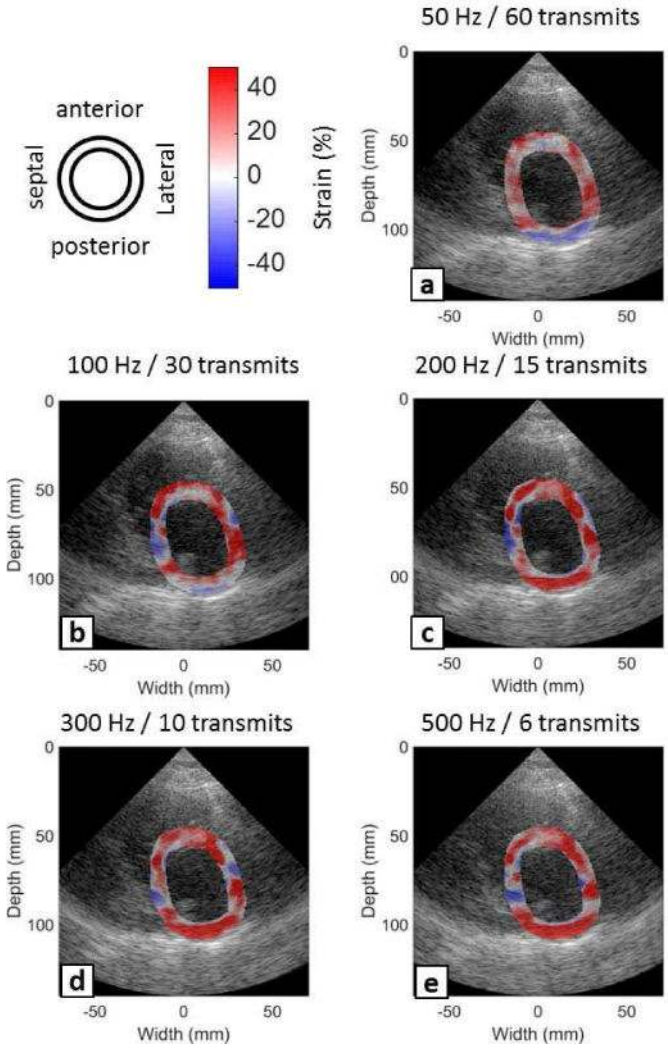

Fig. 7.

Left ventricular cumulative radial strains acquired via transthoracic imaging with steered compounding at 3000 PRF. Five frame rate/transmit number configurations were investigated. As the subject was healthy, it was expected that the transthoracic parasternal short axis view should yield homogenously positive strain. Strain estimated with frame rate configurations of 200 Hz to 500 Hz (b–e) were similar, indicating good myocardial healthy as anticipated. In contrast, the 100 Hz (b) and 50 Hz (a) configurations have defined areas of negative/zero strain in the anterior and posterior, erroneously suggesting ischemia in those areas of the heart.

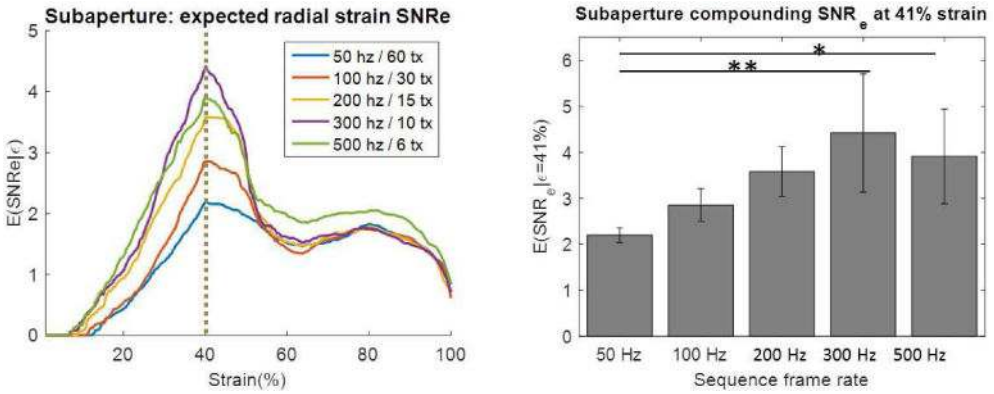

Fig. 8.

Strain estimation accuracy of subaperture compounding in transthoracic imaging of five healthy subjects was determined with the strain filter. The average E(SNRe|ε) over five subjects from 1% to 100% strain is shown (a). The expected SNRe of each frame rate configuration at 41% strain (denoted by brown dashed line), at approximately which the strain estimator yields the most accurate, was statistically compared with a one-way ANOVA and Tukey-Kramer multiple comparison test (b). The 500 Hz configuration is significantly more accurate compared to 50 Hz ($p<0.05$); the 300 Hz configuration is likewise more accurate compared to 50 Hz, but at a higher significance level ($p<0.01$).

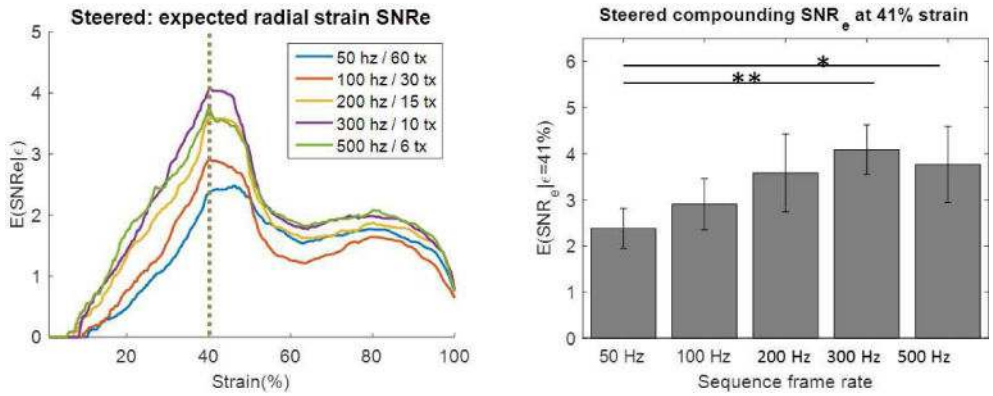

Fig. 9.

Strain estimation accuracy of steered compounding in transthoracic imaging of five healthy subjects was determined with the strain filter. The average E(SNRe|ε) over five subjects as a function of strain from 1% to 100% strain is shown (a). The expected SNRe of each frame rate configuration at 41% strain (denoted by brown dashed line), at approximately which the strain estimator yields the most accurate strains, was statistically compared with a one-way ANOVA and Tukey-Kramer multiple comparison test (b). The 500 Hz configuration is significantly more accurate compared to 50 Hz ($p<0.05$); the 300 Hz configuration is likewise more accurate compared to 50 Hz, but at a higher significance level ($p<0.01$).

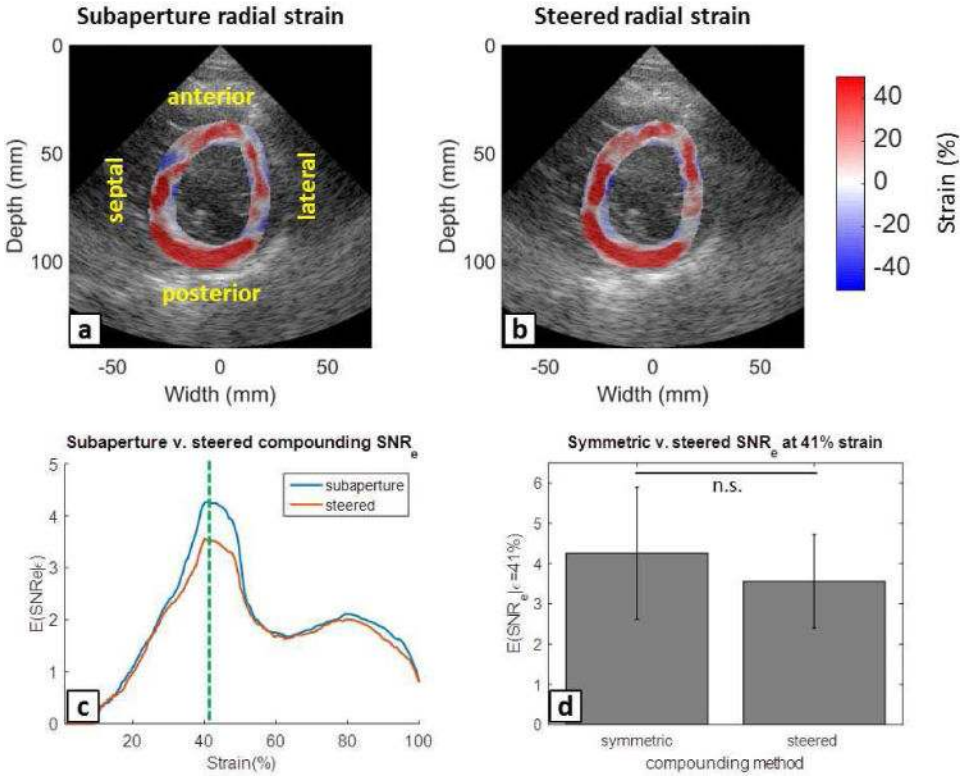

Fig. 10.

Subaperture and steered compounding were compared by transthoracic imaging of five healthy subjects. Cumulative radial strains were similar, showing homogenous positive strain throughout (a–b). The average E(SNRe|ε) over five subjects as a function of the common log of strain from 1% to 100% strain is shown (b). Inspection of the strain filter results (c) seem to suggest that subaperture compounding estimates strain more accurately within ε = 30%–50%. However, using the t-test to compare SNRe at 41% (denoted by green dashed line), which is approximately at which the strain estimator yields the more accurate strains, indicates that there is no significant difference in the strain estimation accuracy of the two methods (d).

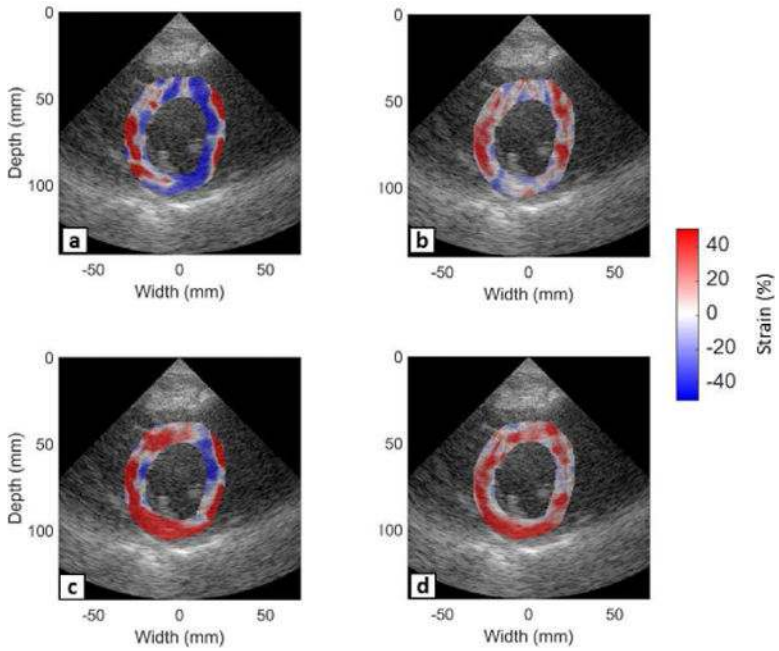

Fig. 11.

Strain estimation accuracy with and without downsampling prior to lateral displacement estimation. A steered compounding sequence at 500 Hz was used to image the myocardium of a healthy subject at the parasternal short axis view. Lateral displacement estimation was performed at 500 Hz, leading to artifacts that were especially prominent in the endocardial lateral wall (a). Downsampling to 100 Hz prior to lateral displacement estimation produces a more physiologically accurate lateral strain distribution (b). The lateral strain has a direct influence on the quality of the radial strain when the lateral estimate is calculated at 500 Hz (c) and 100 Hz (d).

TABLE I

Sonographic SNR (dB)

Frame rate/number of transmits	Subaperture compounding	Steered compounding
500 Hz/6 sources	2.15 ±2.35	2.84± 1.54
300 Hz/10 sources	3.28 ± 1.00	3.45 ± 1.82
200 Hz/15 sources	4.16± 1.26	3.60 ±1.93
100 Hz/30 sources	4.23 ± 1.38	3.59± 1.86
50 Hz/60 sources	3.71± 1.18	3.47 ±2.23